Coarsening of cellular domain patterns in magnetic garnet films

K. L. Babcock,* R. Seshadri, and R. M. Westervelt
Division of Applied Sciences and Department of Physics, Harvard University, Cambridge, Massachusetts 02138
(Received 13 October 1989)

We experimentally study the coarsening of two-dimensional cellular domain patterns in an increasing bias field. As in soap froths and polycrystalline materials, the coarsening is driven by effective cell surface energy. We find that the domain patterns are distinguished by a nonmonotonic change in the total cell surface energy and by topological evolution that proceeds almost exclusively by cell elimination. Aboav's law describing topological correlations between neighboring cells is found to hold over a wide range of bias and cell density. We have also evaluated the distribution $P(n)$ of n-sided cells over three decades in cell density. The patterns show a form of partial scaling: over a two-decade drop in cell density, the fraction of all cells that are pentagonal bubble traps (fivefold symmetric domain structures containing trapped magnetic bubbles) remains nearly constant at $f_5 \approx 0.2$ while $P(n)$ changes rapidly. The partial scaling may be related to a novel topological structure in which the bubble traps act as stable fivefold vertices.

I. INTRODUCTION

Two-dimensional cellular patterns exhibit an intriguing competition between order and disorder, wherein an appearance of randomness arising from a variety of cell shapes and sizes is balanced by underlying topological constraints.[1] In evolving cellular systems such as soap froths and polycrystalline grain growth, this competition combines with the relatively simple dynamics of individual cells[2] to produce very subtle overall structure and evolution. On account of its experimental accessibility and relative simplicity, the two-dimensional soap froth has traditionally served as the prototype for grain growth and other evolving cellular structures. Several recent experimental[3,4] and theoretical[5–9] treatments and computer simulations[10–12] of soap froths have attempted to characterize the rate of coarsening, topological correlations and disorder, and correlations between cell size and shape.

Cellular domain patterns in magnetic garnet films stand as a cellular system with a diverse but little-explored phenomenology. In response to a spatially uniform magnetic bias field H_B, cells with fewer than six sides contract and vanish, and the patterns coarsen in a manner comparable to soap froths. We described in Ref. 13 how magnetic field and domain wall energies give rise to effective tension in the stripe domains that comprise the cell boundaries. The stripe tension drives the pattern evolution, and provides a link between the domain patterns and the surface-energy driven soap froths and granular structures.

In this paper we pursue the experimental characterization of cellular domain patterns coarsened by a monotonically increasing bias field. Specifically, we study patterns evolved at room temperature from an initial, $H_B = 0$ state consisting of a disordered sea of magnetic bubbles. As shown in Fig. 1, aligning the bias field with the bubble magnetization and increasing its magnitude produces a sequence of cellular configurations whose average cell density decreases smoothly and monotonically. (This frothlike evolution contrasts with the two-phase "melting" transitions that result from ordered lattices of magnetic bubbles.[14]) The observations described here concern energetic and topological aspects of the domain patterns as a function of bias field.

One goal of this paper is to clarify the nature of the domain pattern energetics. The patterns are governed by three energy components: the domain wall energy, the energy contained in the demagnetization fields that originate in the magnetization, and the energy of interaction between the magnetization and the external bias field H_B. We present measurements of the area densities of the domain wall and bias-magnetization interaction energies obtained by computer analysis of digitized pattern images. These components add to the demagnetization energy to produce tension in the stripe domains that comprise the cell boundaries.[13] By combining an analytic approximation for stripe tension with measurements of the domain wall length, we estimate the total cell surface energy that effectively drives the pattern evolution. The bias dependence of the stripe tension leads to *non*monotonic change in the total cell surface energy concurrent with the monotonic decrease in cell density.

We have also evaluated statistical quantities conventionally used to describe the topological structure of cellular patterns. In particular, we studied the evolution of the distribution $P(n)$ of cells with n sides, and its second moment μ_2, over a nearly three-decade drop in cell density. Following Aboav,[15,16] Weaire,[17] and others, we also examined topological correlations between neighboring cells by way of the quantity $m(n)$, the average number of sides of neighbors of n-sided cells.

Much of the energetic and topological character of the domain patterns is dominated by pentagonal bubble traps, fivefold symmetric domain structures that contain trapped magnetic bubbles. Bubble traps are described in detail in Refs. 13 and 18; many can be seen in frames (d)

and (e) of Fig. 1. Bubble traps are formed by the contraction of five-sided cells, and resist the complete collapse favored by stripe tension. This obstruction to the topological evolution prevents the patterns from maintaining a cell density that minimizes the total pattern energy as H_B is increased.[13] As a result, the patterns remain far from equilibrium throughout the *high-tension* bias regime $H_{RI} < H_B < H_5$, where H_{RI} is the run-in field of stripe domains,[19] and H_5 is the maximum bias field in which isolated bubble traps can survive. In this regime, all stripe segments are under tension, and fixing the bias allows the patterns to settle into stationary configurations characterized by tension balanced at the vertices and bubble traps where the stripe segments join. While bubble traps do not survive to $H_B > H_5$, patterns of finite cell density persist because coercive friction hinders coarsening.[13]

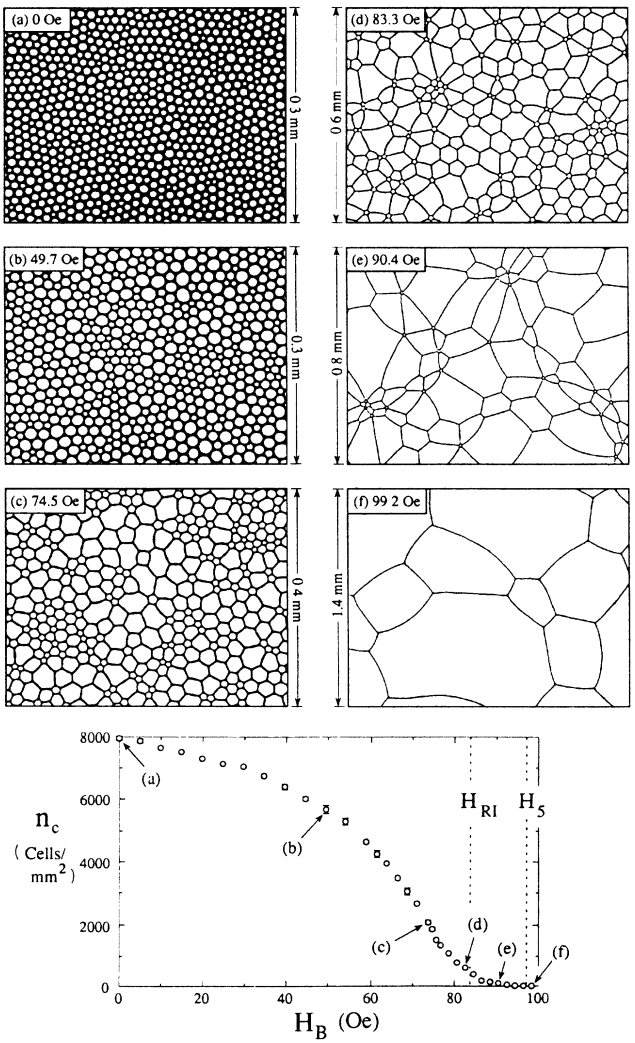

FIG. 1. Cell density vs bias field, and corresponding digitized photographs of patterns at selected bias field, described in the text. White (black) areas correspond to magnetization aligned with (against) H_B. Dashed lines bound the high-tension regime, where H_{RI} is the run-in field of stripe domains, and H_5 is the collapse field of isolated bubble traps.

We devote particular attention to the two-decade drop in cell density that occurs in the high-tension regime. The measured average cell density obeys a power law in the bias field $n_c \propto (H_5 - H_B)^{\alpha}$ with $\alpha = 2.9$, where the exponent α is strongly influenced by nonlocal domain interactions and bunching in the local cell density. Throughout the high-tension interval, the bubble traps are much smaller than the average cell size, and they act as stable fivefold vertices. This contrasts with previously studied experimental cellular systems, which are all *froths* comprised exclusively of threefold vertices. It is well known that froths are subject to the topological constraint[1] $\langle n \rangle = 6$. This constraint is altered in a more complex structure containing both threefold and fivefold vertices, and we discuss the implications of Euler's relation in the case of the domain patterns. The central role of the bubble traps is underscored by our observation that the fraction of all cells that are bubble traps remains nearly constant over a significant drop in cell density, a phenomenon reminiscent of the dynamic scaling that has excited recent interest in soap froths.[4]

Cellular domain patterns in garnet films are well suited for experimental examination. The accessibility of the domain patterns rivals that of soap froths: their magneto-optical properties allow direct, room temperature observation using standard optical techniques, and the bias field affords precise control of the pattern evolution. Fixing the bias allows the patterns to settle into stationary configurations that can be studied at leisure. The patterns contain enough cells (several million in the zero-bias configuration) that boundary effects, which often plague experiments and simulations of cellular systems, are negligible. High-contrast domain images allow digitization and automated compilation of statistical data, thus minimizing tedious manual counting of large numbers of cells.

The remainder of the paper is divided into six sections. Section II describes the garnet film used for our observations and the techniques used to nucleate, control, record, and analyze the domain patterns. An overview of the pattern coarsening and energetic bias regimes is provided in Sec. III. Section IV presents measurements of energy components of the patterns, and describes a complementary estimate of the total, effective cell surface energy. Section V considers topological aspects of the evolution, including the distribution $P(n)$ of n-sided cells and its second moment, and Aboav's law of topological correlations between neighboring cells. Sec. VI discusses the coarsening and topological structure of the nonequilibrium patterns that populate the high-tension bias regime $H_{RI} < H_B < H_5$, with particular attention devoted to the role of the pentagonal bubble traps. Finally, Sec. VII summarizes our observations.

II. MATERIAL PROPERTIES AND PROCEDURE

Our observations focused on a garnet film formulated at the Airtron Division of Litton Industries for magneto-optic device applications; this film is described in detail elsewhere.[13,18,20] Briefly, the film has material composi-

tion $Fe_{3.91}Y_{1.20}Bi_{1.09}Gd_{0.95}Ga_{0.76}Tm_{0.09}O_{12}$, bulk magnetization $4\pi M = 190$ G, thickness $t = 7.8$ μm, and Curie point $T_{Cur} = 170$ °C. Typical of device-oriented garnets, the film has strong uniaxial magnetic anisotropy with easy axis perpendicular to the film plane. The anisotropy supports vertical domain walls that separate "up" and "down" domains (those comprised of magnetization aligned with and opposite to H_B, respectively). The domain walls are narrow (~ 0.1 μm) compared to the domain sizes (~ 10 μm), and have an effective surface energy $\sigma_W = 0.23$ erg/cm^2. The patterns are essentially two dimensional, and evolve by the lateral translation of the domain walls. The material properties and domain structure of garnet films are discussed extensively in the literature.[19,21,22]

Although this paper concerns observations of the Airtron garnet, we expect the general results to also apply to other device-oriented films. Garnet films with similar values of the ratio $\sigma_W/4\pi M^2 t$ ($=0.104$ in the Airtron garnet) possess similar domain configurations when lengths are scaled to units of film thickness t and fields in units of $4\pi M$.[13,22] Indeed, we have observed frothlike coarsening qualitatively identical to that described here in each of four additional films with ratios $0.09 < \sigma_W/4\pi M^2 t < 0.13$. Most device-oriented garnet films lay in or near this range.

The domain patterns were observed via standard optical microscopy by utilizing the Faraday rotation of transmitted polarized light with an analyzer oriented to give contrast between the up and down domains. The Airtron garnet film was designed to accommodate a large amount of bismuth,[20] yielding an unusually large figure of merit (ratio of magneto-optic rotation to absorption) and exceptionally bright, high-contrast domain images. The images were recorded as high-contrast Polaroid photographs, which were then digitized on a flatbed scanner at a resolution of 300 dots per photograph inch, equivalent to $\sim 1-10$ dots per 1 μm of garnet film depending on microscope magnification. The fidelity of the digitized images was limited primarily by the clarity of the photographs, and not by the digitizing resolution. In all digitized photographs shown in the figures, the white (black) areas correspond to up (down) magnetization.

Many of the measurements were performed by computer analysis of 1 bit (black and white) digitized pattern images. Programs were written to exploit the graphics-oriented design of the Macintosh II. We designed algorithms to accurately determine the domain wall length per unit area L_W, the fraction of area f_d occupied by down magnetization, and the area and number of sides of individual cells.[18] Evaluations of the side distribution $P(n)$ and the neighbor distribution $m(n)$ were partially automated so as to count thousands of cells. The error rate of the side-counting algorithm became unacceptable at large bias fields, where irregular cells shapes and low cell densities made suitable digitized images difficult to produce. Fortunately, the manual counting required to complete the analysis was a manageable task.

For the data presented here, the initial (zero bias) states were disordered bubble seas nucleated via saturation and removal of an in-plane magnetic field. The properties of the bubble sea were reproducible and uniform throughout the film, with cell density 7900 ± 80 bubbles/mm^2. Several million bubbles populated the usable, low-defect area (~ 3 cm^2) of the film at $H_B = 0$ and ~ 1000 cells remained when the bias passed through the bubble trap collapse field H_5. Film boundaries and defects had a negligible effect on the results. Bias was raised monotonically in increments $\Delta H_B < 0.5$ Oe. After each increment, the patterns were allowed ample time to settle into new stationary configurations which were photographed as required. Unless otherwise noted, descriptions and analysis concern stationary patterns. Measurements typically represent an average of the results of multiple sweeps of bias field from the reproducible zero-bias bubble seas. An ac field component (frequency 40 Hz, amplitude 7 Oe) was applied in addition to the dc bias to minimize the effects of coercive friction and smooth the domain wall motion; this technique and the ac configuration are discussed in Refs. 13 and 18. Many of the topological characteristics described in Secs. V and VI rely on the presence of the ac field.

III. OVERVIEW OF COARSENING

Figure 1 shows the monotonic decrease in the average cell density n_c ad H_B is increased from zero through the bubble trap collapse point $H_5 = 98.5$ Oe. (We abbreviate the more precise notation H_5^{ac} of Ref. 13; the value given is the largest bias to which bubble traps survive with the ac field applied.) A description of the associated photographs will serve as a preview of later sections. Frame (a) shows the initial disordered sea of magnetic bubbles. In Fig. 1(b), the pattern retains the character of a bubble sea, with the increased bias causing the bubbles to expand and press on one another. From (a) to (b), n_c decreases by the collapse of bubbles with fewer than six nearest neighbors as they are squeezed by the growth of the larger bubbles. The mechanism of collapse is energetically similar to the destabilization of pentagonal bubble traps.[18] In Fig. 1(c), a cellular structure has formed with well-defined stripe segments and vertices, and bubble traps have begun to appear. Frame (d) is near the crossover to the high-tension regime at the stripe run-in field H_{RI}. Spatial inhomogeneity (bunching) in the cell density is marked. (The bunching is intrinsic to the pattern structure, and is not caused by film nonuniformity.) The bubble traps begin to inhibit the topological evolution, and the patterns can no longer maintain a cell density that minimizes the total energy. Some stripe segments are under tension, while other regions of the pattern are relaxed, as indicated by the stable, regular (pentagonal) five-sided cells. Configuration (e) is near the center of the high-tension regime, described in detail in Ref. 13. All stripe segments are under tensions that are balanced at the bubble traps and threefold vertices. The bubble traps are much smaller than the average cell size, and act as stable fivefold vertices. Bunching in the cell density is at a maximum; note the knots of high cell density held together by the bubble traps. Increments in H_B destabilize these traps, triggering "avalanches" of cell eliminations that propagate through the pattern and release tension.

In the stationary patterns in this regime, five-sided cells other than the bubble traps are irregularly shaped (i.e., not pentagonal), and three-sided cells are absent. Four-sided cells are observed only in the upper half of the regime. In Fig. 1(f), $H_B > H_5$, all bubble traps have vanished, and the patterns appear similar to soap froths. Reversed magnetization remains only because of coercive friction that hinders the lateral motion of the long stripe segments. Further increase in H_B destabilizes cells of increasing size as the combination of bias and ac field tolerate progressively less curvature in the stripe segments.[13,18] The rate of cell elimination $\partial n_c/\partial H_B$ is very low, and the patterns survive to $H_B = H_V \approx 151$ Oe, where H_V is the bias field at which the remaining vertices are pinched off and the cellular structure is destroyed.[13]

As shown in Fig. 1, the cell density $n_c(H_B)$ is divided into two regions: concave down at low bias, and concave up at higher bias, with inflection at $H_B \approx 75$ Oe. As discussed in Ref. 13, the spacing d_s in minimum energy stripe patterns[23] near H_{RI} obeys a power law $s_s \propto (H_{RI} - H_B)^{-\beta}$, with exponent $\beta \approx \frac{1}{2}$. Using the correspondence $1/d_s^2 \leftrightarrow n_c$, similar arguments would predict power-law behavior for minimum energy cellular paterns of the form $n_c \propto (H_{RI} - H_B)^{\alpha}$, with $\alpha \approx 1$. The experimental observation of an inflection point in n_c instead of a linear approach to zero cell density suggests that the patterns begin to be pushed away from equilibrium near this point. This conjecture is supported by the onset of bunching of the cell density near the inflection point. Because stripe tension increases with the amount of stray field generated by down magnetization, which in turn increases with cell density,[13] the stripe segments in regions of high cell density are probably under tension for H_B greater than the inflection point.

Thus we slightly refine our previous outline[13] of the bias regimes. For $H_B \lesssim 75$ Oe, the patterns remain close to equilibrium, characterized by small or zero stripe tension. In the interval 75 Oe $< H_B < H_{RI}$, some stripe segments are under tension, bunching in the cell density becomes noticeable, and the patterns begin leaving equilibrium. The high-tension regime $H_{RI} < H_B < H_5$ is distinguished by nonequilibrium patterns in which *all* stripe segments are under tension. The bias dependence of the cell density in this regime is discussed in Sec. VI.

IV. ENERGETICS

This section examines the bias dependence of individual energy components, and uses measurements of the total domain wall length to estimate the total energy contained as stripe tension, the analog of the surface free energy of soap froths.

We measured two components of the total energy by computer analysis of digitized pattern images. The fraction of down magnetization f_d (determined by the area of the dark regions in the figures) and the length of domain wall per unit area of the garnet L_W are plotted in Fig. 2(a) versus bias field. The fraction f_d decreases monotonically. The domain wall length L_W at first shows a (barely visible) increase because the expansion of the bubble

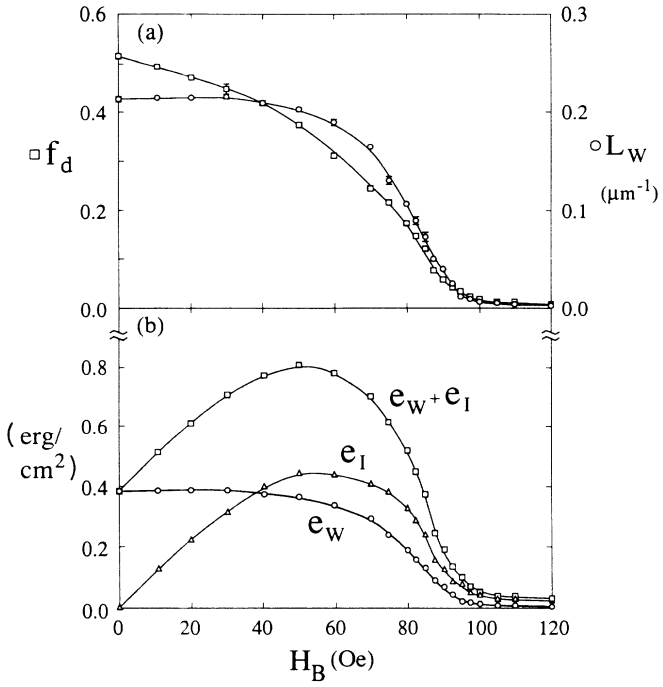

FIG. 2. (a) Fraction of down magnetization and domain wall length per unit area of garnet film vs bias field. (b) Interaction and domain wall energies per unit area and their sum, relative to saturation. Solid curves are guides.

radii initially dominates the decrease in f_d. The interaction and wall energy densities are then given by $e_I = 2MH_B t f_d$ and $e_W = \sigma_W t L_W$ (erg/cm^2); these energies and their sum are shown in Fig. 2(b). (*Energy density* here refers to the energy per unit area of garnet, averaged over a large region of the pattern.) Following convention, all energies are measured as the difference from saturation, i.e., a single-domain state with all magnetization aligned with H_B. Both e_I and e_W remain positive until all cells are destroyed at $H_V \approx 151$ Oe.

The remaining ingredient of the total energy is the demagnetization energy density $e_D = H_D^2/8\pi$, where H_D is the demagnetization field, i.e., the field that originates in the magnetization. More precisely, field lines of H_D originate at the film surface, where $\nabla \cdot \mathbf{M} \neq 0$. Relative to saturation, e_D is negative so long as cells, and hence down magnetization, remain. Measurement of e_D is difficult because H_D strays outside of the garnet, and calculations of the total demagnetization energy are hampered by its nonlocal form.[19,24] The total energy is thus difficult to determine experimentally.

However, in the high-tension regime we can use the data plotted in Fig. 2 to estimate the total energy by utilizing the connection between the energy components and the stripe tension.[13] This connection underlies the well-known analytic form for the tension, equivalent to the energy per unit length $E_s(H_B)$, calculated for an *isolated* stripe domain relative to saturation.[13,24] The function $E_s(H_B)$ increases nonmotonically with bias, crossing zero at the stripe run-in field H_{RI}, and reaching a maximum at

$H_B = 4\pi M$ equal to the energy contained in the two domain walls. The total energy per unit area of the cellular patterns can be estimated as $e_{tot}(H_B) \approx E_s(H_B)[L_W(H_B)/2]$. Here $L_W/2$ is a measure of the stripe length per unit area, where L_W is the experimentally determined domain wall length per unit area shown in Fig. 2(a); the factor of $\frac{1}{2}$ accounts for the two domain walls bounding each stripe. This measure is fairly accurate for the sparse patterns in the high-tension regime. The result for e_{tot} is shown by the data markers in Fig. 3. (The solid curve is a schematic representation of the energy in excess of equilibrium e_{ex}, described below.) The energy e_{tot} rises to a peak near $H_B \approx 90$ Oe as the increasing stripe tension dominates the product, and then falls away as the froth coarsens and the cell boundary length is reduced. Note that, because the negative demagnetization energy balances the positive domain wall and interaction energies, the stripe energy E_s, and hence the maximum value of e_{tot}, are only a small fraction of the magnitude of the individual components. The energy barriers between domain configurations are nonetheless much greater than kT_{room},[13,18] and the patterns observed in the high-tension regime are nonequilibrium, metastable states.

The use of the isolated stripe energy E_s in the above estimate of e_{tot} ignores the effect of domain interactions in the real pattern. The total energy is thus underestimated because, for given H_B, stripe tension increases with cell density.[13] The zero crossing of e_{tot} is artificially imposed at H_{RI} by the crossing of E_s, whereas some stripes in the actual patterns have positive tension below H_{RI}, as mentioned in Sec. III. However, incorporating interactions does not change the magnitude of e_{tot} drastically,[13] and the general form of e_{tot} as shown in Fig. 3 is certainly correct.

The expression $e_{tot} \approx E_s(L_W/2)$ mimics the form (surface tension)×(cell boundary length) that gives the total

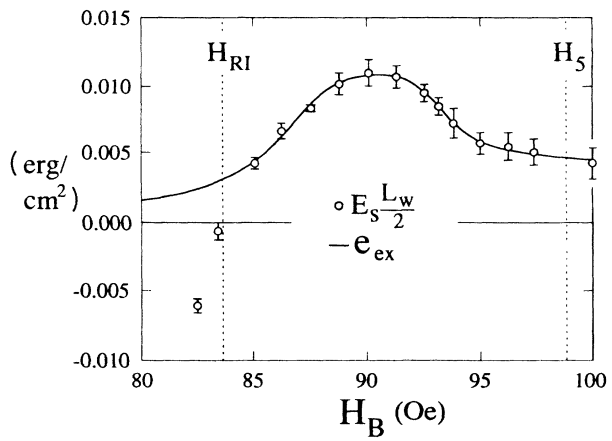

FIG. 3. Data markers indicate the "surface" energy estimate $e_{tot} = E_s(L_W/2)$, where E_s is the calculated tension of an isolated stripe domain, and L_W is the experimental value for the domain wall length per unit area from Fig. 2(a). The solid curve is the schematic form of the energy in excess of equilibrium, with a peak near the center of the high-tension regime (bounded by the dashed lines).

energy of surface-energy driven systems such as soap froths and polycrystalline materials. However, to be precise, we should compare the total pattern energy in excess of equilibrium e_{ex} sketched as the solid curve in Fig. 3, as opposed to the estimate e_{tot}, which used the saturated state as an energy reference. Because for $H_B > H_{RI}$ saturation *is* the equilibrium state,[13] the energy $e_{tot} \approx E_S(L_W/2)$ provides an adequate estimate of e_x in the high-tension regime $H_{RI} < H_B < H_5$, and the curve was simply drawn through the data markers. The form of e_{ex} near to and below H_{RI} was sketched so as to take into account the departure of the patterns from equilibrium near $H_B \approx 75$ Oe. The energy e_{ex} remains close to, but slightly greater than, the equilibrium energy until a few oersteds below H_{RI}. It then rises as the bubble traps inhibit the evolution and stripe tension appears, deviating farthest from equilibrium near the midpoint of the high-tension regime, and finally decays slowly at large bias $H_B > H_5$.

A clear comparison of the energetics of the domain patterns and other cellular systems is now possible. The domain pattern energetics are generally more complex than that of soap froths due to the bias and configuration dependence of the multiple energy components and of the stripe tension. For H_B sufficiently below the run-in field, the patterns adjust to keep the stripe tension, and hence the total effective surface energy e_{ex}, small or negligible. Thus, unlike soap froths, the domain patterns at low bias are not a manifestly nonequilibrium system. However, the nonequilibrium domain patterns in the high-tension regime are characterized by tension in the cell boundaries that is statically balanced at the vertices and bubble traps; see Fig. 1(e). Soap froths share this general feature, but the stable *fivefold* vertices in the form of bubble traps are unique to the domain patterns. The increasing stripe tension in the high-tension regime competes with the decreasing cell density, and the total, effective surface energy changes *non*monotonically as the patterns coarsen. In contrast, the uniform and time-invariant surface tension of soap froths implies a total surface energy proportional to the total cell boundary length, and both the cell density and energy monotonically decrease in time.

V. TOPOLOGICAL DISORDER AND CORRELATIONS

This section describes the local topological mechanisms by which cellular domain patterns evolve, and presents experimental evaluations of statistical distributions conventionally used to describe topological structure in cellular patterns.

Typical of systems driven by cell surface energy, the local topological evolution of the domain patterns follows the rule[2] that cells with fewer than six sides tends to contract. However, we find two constraints to apply that are unusual among cellular systems. (i) Over the entire range of bias field $0 < H_B < H_V$, we observe no neighbor switching, i.e., processes in which local cell neighborhoods are rearranged but the total numbers of sides, cells, and vertices are conserved. (Such topological changes are often referred to as "$T1$" processes in the literature.[1]) Instead, we find that the vanishing of cells ("$T2$" processes) is the essential mechanism of topological change. Exceptions

occur only for bias fields at or above the center of the high-tension regime, and then only rarely, when cell walls are severed as the size of a contracting four-sided cell approaches zero. The lack of neighbor switching is significant in that this process provides a mechanism for strain relief.[25] (ii) Cells with fewer than five sides are extremely rare in the stationary patterns, except near the upper end of the high-tension regime. Cells with $n<5$ are often formed during the course of the evolution when, for example, the vanishing of a cell removes a side from a neighboring five-sided cell. However, these cells tend to be unstable and collapse immediately, and are observed only rarely in the stationary patterns.[26] Except near the upper end of the high-tension regime, five-sided cells thus provide the sole topological balance required to satisfy $\langle n \rangle = 6$, a constraint imposed on all two-dimensional cellular patterns with vertices of threefold coordination.[1] (Throughout this section, pentagonal bubble traps are considered as five-sided cells.) The largest n increases from $n_{\max}=8$ in the initial bubble sea to $n_{\max}=11$ or 12 in the high-tension regime. Cells with $n>12$ are extremely rare. These observations rely on the presence of the ac field. For example, in its absence, the breaking of cell walls is common,[13] and can result in cells with n as large as 30.

Topological disorder in cellular patterns is conventionally measured by the second moment

$$\mu_2 = \sum_n P(n)(n-6)^2 = \langle (n-\langle n \rangle)^2 \rangle , \quad (1)$$

where $P(n)$ is the fraction of cells with n sides. The bias dependence of μ_2 is shown in Fig. 4(a). For bias fields up into the high-tension regime, μ_2 was determined by computer analysis of the digitized pattern images as described in Sec. II. At larger bias fields, the low cell density and irregular cell shapes necessitated counting by hand. In all but the sparsest patterns, a minimum of several hundred cells, and often thousands, were sampled to determine $P(n)$ at each bias value. Enough cells were included to ensure that $|\langle n \rangle - 6| < 0.1$ for all samples. (The tolerance was, in fact, much better in most cases.) The second moment μ_2 remains smaller than unity for more than a two-decade drop in the cell density n_c, during which the nature of the patterns changes from a bubble sea to a nonequilibrium, minimal surface pattern. The second moment plateaus and dips slightly over $H_B \sim 75-85$ Oe as the patterns begin to move away from equilibrium. Only when H_B reaches the upper half of the high-tension regime does μ_2 increase rapidly. However, μ_2 does not diverge as $H_B \to H_5$, and, in fact, does not appear to become much larger than the maximum value $\mu_2 \approx 3$ shown in Fig. 4(a).[27] Low cell density and lack of reproducibility due to coercivity make μ_2 difficult to determine above H_5. Occasional severing of the stripe segments in the high basis regime $H_B > H_5$ sometimes produces cells of large n that inflate μ_2.

Over nearly a three-decade drop in cell density, the toplogical disorder as measured by μ_2 remains significantly smaller than the value $\mu_2 \approx 1.4$ observed in mature soap froths.[4] The near absence of three- and four-sided cells in the stationary domain patterns slows the generation of topological disorder and suppresses the tails of $P(n)$. The appearance of four-sided cells and an increase in $P(5)$ contributes to the rise in μ_2 in the upper half of the high-tension regime.

The side distributions $P(n)$ are shown in Fig. 4(b) for patterns roughly a decade apart in cell density. The average topological structure changes only slightly from $H_B=0$ to H_{RI}, as indicated by side distributions (1)–(3), and the change in μ_2 is correspondingly small. The cell density drops by a factor of ~ 20 over this bias range as the patterns transform from bubble seas to fully developed cellular patterns containing bubble traps. The near invariance of $P(n)$ is reminiscent of the dynamic scaling of soap froths.[4] However, it is unclear how to compare the *time* evolution of the soap froth, in which the surface tension does not change, with the evolution of the transforming domain patterns governed by bias-dependent stripe tension. The side distributions $P(n)$ of the domain patterns change most rapidly through the high-tension regime, as indicated by curves (3)–(5) in Fig. 4(b), and reflected by the rapid rise in μ_2.

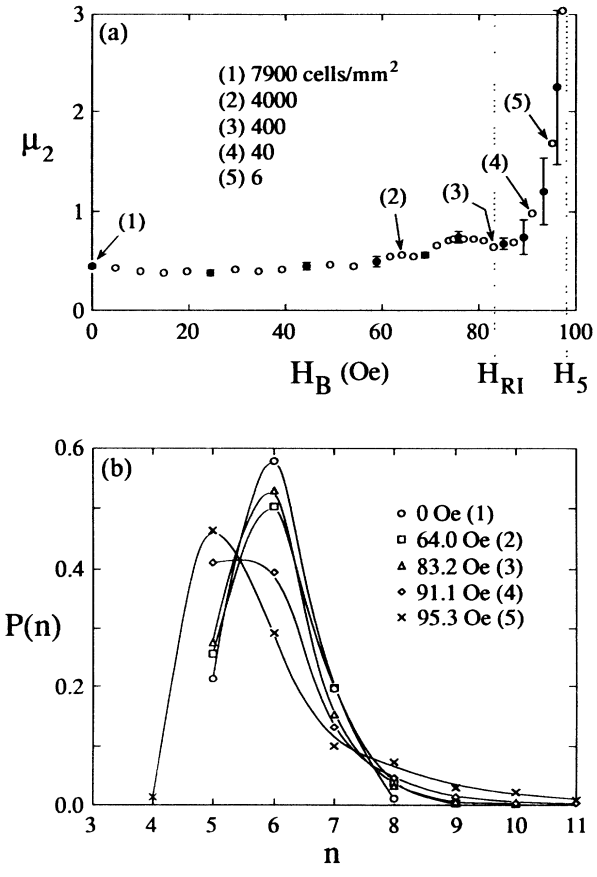

FIG. 4. (a) Second moment of the side distribution $P(n)$ vs bias field. Cell densities at selected bias values are indicated. Representative standard deviations for three bias sweeps are shown for the closed circles. The dashed lines bound the high-tension regime. (b) Side distribution at selected bias fields. Cell densities and second moments correspond to points (1)–(5) labeled in (a).

We examined topological correlations by means of the quantity $m(n)$, the average number of sides of neighbors of n-sided cells. The primary aim was to test Aboav's law

$$m(n)=6-a+\frac{6a+\mu_2}{n}\ , \tag{2}$$

which has been found to hold for a number of cellular systems.[1,4] The free parameter a has been conjectured to reflect the processes that drive the coarsening. Equation (2) can be derived[16] by assuming the form $m(n)=A+B/n$, which describes many (but not all) two-dimensional cellular structures, and using the rigorous topological sum rule[17]

$$\sum_n nm(n)P(n)=36+\mu_2 \tag{3}$$

to relate the parameters A and B via the independently measured second moment μ_2. We determined $m(n)$ for the domain patterns at multiple bias values by means of image analysis (again with some manual counting at low cell densities), employing methodology similar to that used to evaluate $P(n)$. The results for two widely separated bias values are shown by the data markers in Fig. 5(a). The solid curves represent Aboav's law using experimental values for the second moments. The $H_B=0$ bubble sea is accurately described by Aboav's law Eq. (2) with the free parameter $a=1.5$, while at $H_B=89$ Oe, in the heart of the high-tension regime, the data are best fit by $a=1.2$. Figure 5(b) verifies that the linear relation between nm and n, as well as Aboav's law, hold very well. Patterns at intermediate bias also obey Aboav's law, with some a actually smaller than the values corresponding to Fig. 5. For example, $a=0.82$ applies to patterns near $H_B=74$ Oe.

The value $a=1.2$ for the high-tension patterns agrees well with the values $a=1.2$ and 1 found for soap films,[4,16] and the value $a=1$ found to hold for certain polycrystalline materials.[15] The similarity in a is remarkable given the different topological and geometrical structures of these systems. For example, correlations between cell areas and numbers of sides, an important consideration in the filling of the plane by cells, are clearly different for soap froths and domain patterns, given that three- and four-sided cells are virtually absent in the domain patterns, and that the bubble traps are much smaller than the average domain size.

VI. COARSENING IN THE HIGH-TENSION REGIME

Pentagonal bubble traps govern much of the behavior in the high-tension interval $H_{RI}<H_B<H_5$. This section discusses the influence of bubble traps on the observed form of the cell density $n_c(H_B)$, as well as their role as fivefold vertices, an unusual topological structure that distinguishes the domain patterns from other experimental cellular systems.

As shown in Fig. 6(a), the average cell density n_c drops by a factor of ~ 200 over the high-tension regime. The concave-up shape of $n_c(H_B)$ suggests coarsening of the

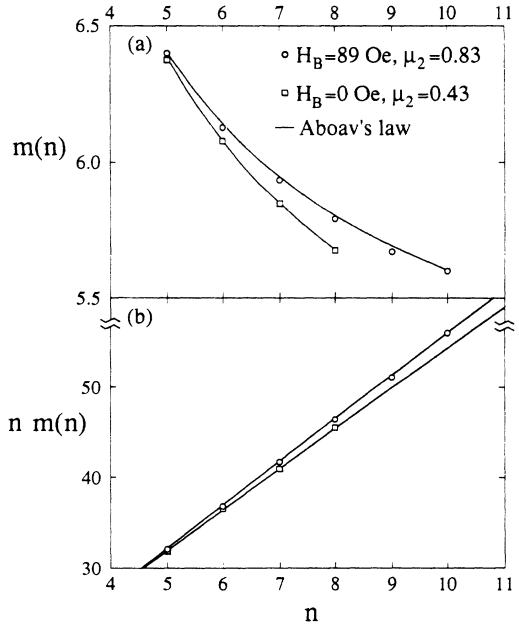

FIG. 5. (a) Average number of sides of neighbors of n-sided cells, at two bias values. The solid curves are Aboav's law with $a=1.5$ for the zero-bias bubble sea, and $a=1.2$ for patterns in the high tension regime. (b) Product of $m(n)$ and n verifying the linear relationship with n and agreement with Aboav's law (lines).

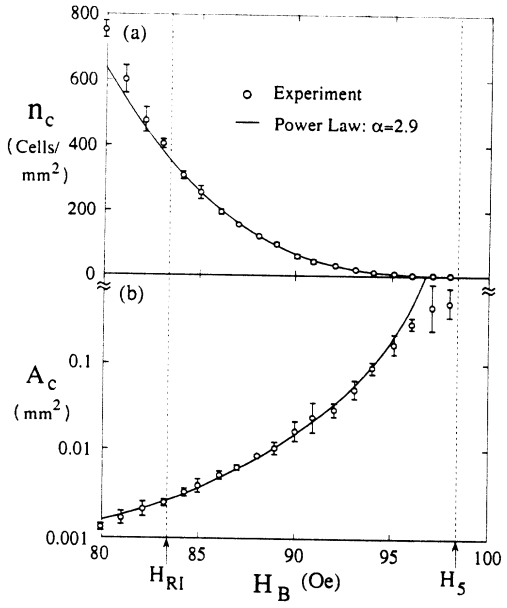

FIG. 6. (a) Cell density in the high-density regime. Error bars are standard deviations for three runs. The solid curve is the power law fit $n_C=C(H_5-H_B)^{\alpha}$, $H_5=98.5$ Oe, and $\alpha=2.9$. (b) Average area per cell $A_c=1/n_c$ plotted on a logarithmic scale vs bias. The data and power law (solid curve) show good agreement for nearly two decades in A_c. The power law $A_c\propto(H_5-H_B)^{-2.9}$ diverges at $H_B=H_5$, whereas the data tails off near H_5 due to coercive friction that hinders coarsening.

form $n_c \propto (H_5 - H_B)^{\alpha}$. The choice of H_5 as the limiting field is motivated by the discussion in Ref. 13 showing that the cell density in an idealized, coercivity-free garnet would be expected to reach zero at H_5. A two-parameter (leading coefficient and exponent) fit to the data with H_5 fixed at its measured value 98.5 Oe gives $\alpha = 2.9 \pm 0.2$; this power law is shown as the solid curve in Fig. 6(a). The average area per cell $A_c = 1/n_c$ is plotted in Fig. 6(b) on a logarithmic scale. The corresponding power-law fit $A_c \propto (H_5 - H_B)^{-2.9}$ shown as the solid curve agrees well with the data over two decades in area or cell density. While the power law for the average cell area diverges as $H_B \rightarrow H_5$, the data tail off as coercive drag hinders the coarsening, and a residual pattern with $n_c \approx 2$ cells/mm^2 remains above H_5 [see Fig. 1(f)]. To our knowledge, the (coercivity-limited) divergence in the average cell size at H_5 is not observed in any other cellular system. (Infinite cell size in soap froths corresponds to time $\rightarrow \infty$.)

In the high-tension regime, bias increments typically destabilize stationary patterns by forcing the collapse of the bubble traps that support them. (As discussed below, bias increments often cause the contraction of cells adjacent to bubble traps, or the contraction of "knots" of cells, but bubble trap collapse is almost always observed to be the first *topological* change.) The form of $n_c(H_B)$ might therefore be expected to rely on the stability criterion for the bubble traps. The approximate condition for the collapse of a given bubble trap is $H_B + H_D^{\text{stray}} = H_5$, where H_D^{stray} is the total demagnetization field originating in reversed magnetization other than that comprising the bubble trap.[18] This additive condition states that H_5 is the total local field required to destabilize the trap. For our purposes, we assume H_5 is constant for the sparse patterns in the high-tension regime. The simplest dimensional argument suggests $H_D^{\text{stray}} \approx Cn_c$, which would give the linear dependence $n_c \sim H_5 - H_B$, i.e., an exponent $\alpha = 1$.

The large deviation of the observed exponent $\alpha = 2.9$ from unity may be related to the notable bunching in the local cell density prevalent in the high-tension interval; see Fig. 1(e). The excess reversed magnetization enhances the stray fields in the bunched regions. Bubble traps in these regions are indeed observed to be the most susceptible to collapse under bias increments. The stability of the pattern is thus limited by the bubble traps that experience the largest stray fields. A condition for *pattern* stability might thus be expressed as $H_B + \max(H_D^{\text{stray}}) = H_5$, where $\max(H_D^{\text{stray}})$ is the largest stray field experienced by *any* bubble trap in the pattern. The inhomogeneities in local cell density imply that $\max(H_D^{\text{stray}}) > \langle H_D^{\text{stray}} \rangle$, the average of the stray fields experienced by the bubble traps. In this picture, the exponent α is determined by the relationship between $\max(H_D^{\text{stray}})$ and the average cell density n_c. The power law indicated by the data in Fig. 6 implies $\max(H_D^{\text{stray}}) \approx Cn_c^{1/\alpha}$, $1/\alpha = 0.34$. This weaker-than-linear dependence may be due to the observed, increasing nonuniformity in the local density as the pattern coarsens through the high-tension regime. However, we have found no compelling explanation for the measured value $\alpha = 2.9$.

The photograph in Fig. 7(a) shows an irregularly shaped five-sided cell neighboring a bubble trap, a common configuration throughout the high-tension regime; see, for example, Fig. 1(e). Stripe tension would favor $T1$ switching of the asymmetric vertices at the narrow end of an irregular cell, as shown schematically in Fig. 7(b). However, $T1$ changes are thwarted by the mutual, approximately dipole-dipole repulsion of the vertices and adjoining stripes, and this process is not observed. The stability of the irregular cells, and of the stationary, nonequilibrium patterns themselves, thus relies on mutual domain repulsion. A sufficient increase in H_B will often destabilize irregular cells so that they contract along their length, as shown schematically in Fig. 7(c). The bubble trap, and often the cell itself, are destroyed in the process.[28]

Figure 8 shows that the fraction f_5 of all cells that are bubble traps versus H_B remains close to $f_5 \approx 0.2$ over the interval $H_{RI} < H_B < \sim 95$ Oe, during which the average cell density n_c drops more than 100-fold. The photographs demonstrate the substantial coarsening over this range. The fraction f_5 drops to zero as $H_B \rightarrow H_5$ in an interval of ~ 3 Oe as the remaining bubble traps become unstable and coercive drag begins to affect the domain motion.

This constancy in f_5 strikingly emphasizes the role of the bubble traps as regulators of the cell density and topological evolution. This phenomenon is somewhat

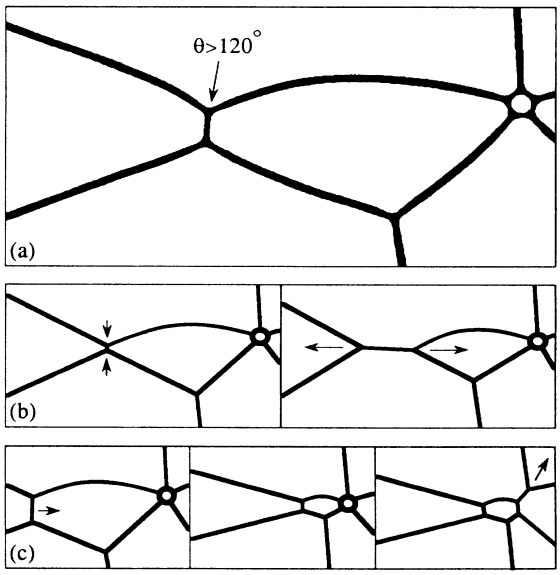

FIG. 7. (a) Photograph of a stable, irregular five-sided cell adjacent to a bubble trap; $H_B = 87$ Oe. (b) Sketch of the $T1$ process and subsequent collapse favored by stripe tension and vertex asymmetry, but which is not observed because of mutual domain repulsion. The stability of the configuration (a) thus relies on domain repulsion. (c) Sketches of observed response to sufficient bias increase. The irregular cell is destabilized and contracts along its length. The bubble trap is destroyed, and in most cases the remaining cell also collapses.

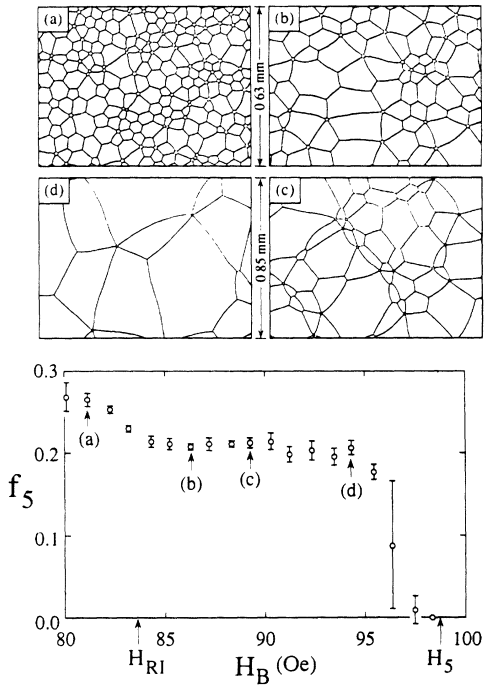

FIG. 8. (a) Fraction of all cells that are pentagonal bubble traps in the high-tension regime, and digitized photographs of corresponding patterns. The fraction f_5 remains close to 0.2 over a nearly two-decade drop in cell density, evidence of partial scaling. Error bars give the standard deviation for three bias sweeps.

surprising in view of the influences of cell bunching and domain repulsion on the pattern stability, the simultaneous rapid change in $P(n)$ and μ_2, and the strong bias dependence of the patterns energetics and effective cell surface tension (Fig. 3) through the high-tension interval. Note in particular that the probability $P(5)$ that a given cell has five sides (including bubble traps) grows significantly over the same bias interval in which f_5 remains constant; compare Fig. 4(b). The constancy in f_5 concurrent with evolution in $P(n)$ might be appropriately described as *partial scaling* to distinguish it from the "complete" scaling observed in mature soap froths, in which the entire distribution $P(n)$ reaches an asymptotic form[4] with $\mu_2 \approx 1.4$.

Underlying the partial scaling may be the fact that, throughout the high-tension regime, the bubble traps are much smaller than the average cell size, and they act as stable fivefold vertices. Viewed this way, the topological structure of the domain patterns differs fundamentally from that of soap films and other froths composed entirely of threefold vertices. We can explore this novel structure by considering the pattern obtained by the mental transformation *bubble trap* $\rightarrow$*fivefold point vertex*. Let the subscript O refer to the original pattern, i.e., the topology in which all vertices are threefold. (In the original pattern, bubble traps are constructed of five threefold vertices, a view held throughout Sec. V.) Let A refer to the alternate pattern topology produced by the transformation. In terms of the fraction f_5 of cells that are bubble traps in the O pattern, it is straightforward to show that the average numbers of sides of the cells in the A pattern is

$$\langle n \rangle_A = \frac{6-10f_5}{1-f_5} , \tag{4}$$

and that the ratio of the number of threefold vertices to fivefold vertices is

$$V_A^3/V_A^5 = 2/f_5 - 5 . \tag{5}$$

(Derivations are given below.) Note that $\langle n \rangle_A < 6$ because neighbors of the bubble traps each lose a side in the transformation. The rigorous topological limits of $f_5 < \frac{2}{5}$ and $\langle n \rangle_A > \frac{10}{3}$ correspond to an A pattern with all fivefold vertices.

It is tantalizing to note that the measured partial scaling value $f_5 \approx \frac{1}{5}$ gives the integral values $\langle n \rangle_A = 5 = V_A^3/V_A^5$. However, there is no obvious topological reason that these quantities must be integral. Given the observed variation in $P(5)$ with H_B in the high-tension regime where f_5 is constant, there seems to be no topological connection between f_5 and $P(5)$. An attempt to understand the observed partial scaling must perhaps incorporate the complex influences of cell density nonuniformity and domain repulsion described above.

The above topological relations can be derived by a straightforward application of Euler's equation. The transformation bubble trap$\rightarrow$fivefold vertex of definition gives $V_A^5 = f_5 C_O$, where C_O is the original number of cells, including bubble traps. The number of threefold vertices after the transformation is then $V_A^3 = V_O - 5f_5 C_O$, because five threefold vertices are "lost" for each bubble trap. In the original pattern $V_O = 2C_O$, leading to the result Eq. (5). To find $\langle n \rangle_A \equiv C_A^{-1} \sum_n n C_A(n)$, where $C_A(n)$ is the number of cells with n sides after the transformation, we can use $2S_A = \sum_n n C_A(n)$, i.e., a segment divides two cells, and $2S_A = 3V_A^3 + 5V_A^5$, because each segment connects two vertices, and the right-hand side is the total number of segments emanating from the vertices. We insert these expressions into Euler's equation for a plane[1]

$$C_A - S_A + V_A = 1 , \tag{6}$$

where $V_A = V_A^3 + V_A^5$, the total number of vertices in the altered pattern. (Euler's equation holds for cellular patterns regardless of the coordination of the vertices.) Using $C_A = C_O(1-f_5)$ gives

$$C_A - \tfrac{1}{2} \sum_n n C_A(n) + (V_A^3 + V_A^5) = 1 = C_A \left[1 - \frac{\langle n \rangle_A}{2} + \frac{2-4f_5}{1-f_5} \right] . \tag{7}$$

In the limit of large C_A, the quantity in large parentheses must approach zero, giving Eq. (4).

VII. SUMMARY AND CONCLUSIONS

In this paper we have experimentally examined several energetic and topological aspects of cellular domain pat-

terns coarsened in an external bias field. Many of our observations demonstrate a strong connection with soap froths and other surface-energy driven cellular systems, while others represent phenomena unique to the domain patterns.

In Sec. IV direct measurements of the domain wall and bias-magnetization interaction energies of cellular patterns were complemented by an estimate of the total energy contained as stripe tension. The nonequilibrium patterns in the high-tension bias interval $H_{RI} < H_B < H_5$ differ from other surface-energy drive patterns in that the bias dependence of the stripe tension leads to a nonmonotonic change in the total, effective surface energy.

Section V examined how the topological structure of the domain patterns evolves over three decades in cell density with increasing bias field H_B. The near absence of three- and four-sided cells in the stationary patterns result in topological disorder that is typically smaller than that of soap froths and other cellular systems. Exceptions occur only beyond the upper half of the high-tension interval. The lack of $T1$ processes prevents five-sided cells from gaining or losing sides, which may also contribute to the relatively small measured value of the second moment μ_2 and to the buildup of strain. The side distribution $P(n)$ changes little from $H_B = 0$ to H_{RI}, during which the patterns evolve from bubble seas to fully developed cellular patterns. Aboav's law of correlations of neighboring cells was found to hold over a range of bias and cell density. The free-parameter value $a = 1.2$ found to hold in the high-tension regime is close to that found for soap froths and polycrystalline materials, and suggests that a near unity might hold generally for systems governed by surface energy, independent of details of their evolution and structure.

The cell density variation with bias $n_c(H_B)$ was found to obey the empirical power law $n_c \sim (H_5 - H_B)^{\alpha}$, $\alpha = 2.9$. The exponent deviates significantly from the value of unity predicted by a simple dimensional argument, possibly because of influences of bunching in the cell density on the stability of the bubble traps that support the patterns. This apparent sensitivity in the coarsening rate $\partial n_c / \partial H_B$ is reminiscent of the large deviation in the observed rate of soap froth coarsening from theoretical predictions.[3,4,16]

The domain patterns exhibit *partial scaling* in the high-tension regime in which the fraction of all cells that are bubble traps remains nearly constant at $f_5 \approx 0.2$ over a two decade drop in cell density. The invariance in f_5 holds while the total fraction of five-sided cells $P(5)$ changes markedly. The partial scaling differs from the dynamic scaling recently observed in soap froths, in which the entire distribution reached an asymptotic form after sufficient maturation.[4]

Viewing the pentagonal bubble traps as fivefold vertices gives rise to a novel topology that is not, to our knowledge, found in any other experimental cellular system. Relative to the usual threefold vertex structure, this topology effectively adds a degree of freedom to Euler's equation, namely, V_A^3 / V_A^5, the ratio of the number of threefold to fivefold vertices. Aspects of this topology may underlie the partial scaling in f_5, and it remains a challenge to theory to examine this topology and possibly explain the observed values $\langle n \rangle_A \approx 5 \approx V_A^3 / V_A^5$.

One aspect of cellular domain patterns that we did not explore is the correlation between cell size and shape. Recent theories[5,7,9] have examined such correlations observed in soap froths,[3] granular structures in metals, and other systems.[1] The small size of the bubble traps produces an unusual configuration that these theories might address. It would perhaps be appropriate to treat the bubble traps as fivefold vertices, and examine correlations in the alternate topology.

We have also not discussed the dynamics of pattern rearrangement that ensue when bias increments destabilize a stationary pattern. In the high-tension regime, the patterns rearrange via "topological avalanches" that propagate through the patterns and lead to long settling times. The avalanches span nearly two decades in size and duration, and may be of relevance to the scenario of self-organized criticality[29] proposed as a mechanism underlying $1/f$ noise; this topic will be addressed in a forthcoming paper.

In conclusion, we have found cellular domain patterns in garnet films to have one of the richest phenomenologies of all cellular systems, with several novel features that extend the conventional scope of cellular pattern study.

ACKNOWLEDGMENTS

We would like to thank Roger Belt and the Airtron Division of Litton Industries for providing the garnet sample, and Raymond Wolfe for valuable discussions. This work was supported in part by the Office of Naval Research under Grants No. N00014-89-J-1023 and No. N00014-89-J-1592.

*Present address: Department of Physics, University of California, Santa Barbara, Santa Barbara, CA 93106.

[1] D. Weaire and N. Rivier, Contemp. Phys. **25**, 59 (1984), the standard view of two-dimensional cellular patterns.

[2] J. Von Neumann, in *Metal Interfaces*, edited by C. Herring (American Society for Metals, Cleveland, 1952), p. 108.

[3] J. A. Glazier, S. P. Gross, and J. Stavans, Phys. Rev. A **36**, 306 (1987).

[4] J. Stavans and J. Glazier, Phys. Rev. Lett. **62**, 1318 (1989).

[5] N. Rivier, Philos. Mag. B **52**, 795 (1983).

[6] C. W. J. Beenaker, Phys. Rev. Lett. **57**, 2454 (1986).

[7] C. W. J. Beenaker, Physica **147A**, 256 (1987).

[8] M. Marder, Phys. Rev. A **36**, 438 (1987).

[9] Rita M. C. De Almeida and J. R. Iglesias, J. Phys. A **21**, 3365 (1988).

[10] D. Weaire and J. P. Kermode, Philos. Mag. B **48**, 245 (1983).

[11] D. Weaire and J. P. Kermode, Philos. Mag. B **50**, 379 (1984).

[12] J. Wejchert, D. Weaire, and J. P. Kermode, Philos. Mag. B **53**, 15 (1986).

[13] K. L. Babcock and R. M. Westervelt, Phys. Rev. A **40**, 2022

(1989).
[14]K. L. Babcock and R. M. Westervelt, Phys. Rev. Lett. **63**, 175 (1989).
[15]D. A. Aboav, Metallography **3**, 383 (1970).
[16]D. A. Aboav, Metallography **13**, 43 (1980).
[17]D. Weaire, Metallography **7**, 157 (1974).
[18]K. L. Babcock, Ph.D. thesis, Harvard University, 1989 (available through University Microfilms International, Ann Arbor, 1990).
[19]A. P. Malozemoff and J. C. Slonczweski, *Magnetic Domain Walls in Bubble Materials* (Academic, New York, 1979).
[20]R. F. Belt and J. B. Ings, SPIE J. **753**, (1987).
[21]*Physics of Magnetic Garnets,* edited by A. Paoletti (North-Holland, Amsterdam, 1978).
[22]A. H. Eschenfelder, *Magnetic Bubble Technology* (Springer-Verlag, New York, 1981), and references therein.
[23]The analytic treatment of Ref. 13 defines the minimum energy stripe or cellular configurations as those corresponding to zero stripe tension.
[24]J. A. Cape and G. W. Lehman, J. App. Phys. **42**, 5732 (1971).
[25]For example, in Ref. 4, Stavans and Glazier report that five-sided bubbles in soap froths undergo direct T2 elimination only 16% of the time, while side loss via T1 processes occurs 50% of the time.
[26]Large numbers of three- and four-sided cells can arise from irregular bubble seas less dense than those used here. However, these cells are eliminated, and the initial state "forgotten," with only a moderate increase in H_B.
[27]This statement defends against a possible inferrence by the reader that the coercivity-limited divergence in average cell area at $H_B = H_5$, described in Sec. VI, might imply a divergence in $\mu 2$.
[28]Exceptions occur at and below the crossover to the high-tension regime, where bubble traps can coexist as neighboring cells; see photograph (d) of Fig. 1. However, bubble trap pairs are not observed in the heart of the regime.
[29]P. Bak, C. Tang, and K. Wiesenfeld, Phys. Rev. Lett. **59**, 381 (1987).